ACS APPLIED MATERIALS & INTERFACES

RESEARCH ARTICLE

www.acsami.org

$LiNi_{1/3}Co_{1/3}Mn_{1/3}O_2$—Graphene Composite as a Promising Cathode for Lithium-Ion Batteries

Chitturi Venkateswara Rao,*,† Arava Leela Mohana Reddy,*,‡ Yasuyuki Ishikawa,† and Pulickel M. Ajayan‡

†Department of Chemistry, University of Puerto Rico, San Juan, Puerto Rico 00931, United States

‡Department of Mechanical Engineering and Materials Science, Rice University, Houston, Texas 77005, United States

Supporting Information

ABSTRACT: The use of graphene as a conductive additive to enhance the discharge capacity and rate capability of $LiNi_{1/3}Co_{1/3}Mn_{1/3}O_2$ electrode material has been demonstrated. $LiNi_{1/3}Co_{1/3}Mn_{1/3}O_2$ and its composite with graphene (90:10 wt %) were prepared by microemulsion and ball-milling techniques, respectively. The structural and morphological features of the prepared materials were investigated with powder X-ray diffraction, scanning electron microscopy, transmission electron microscopy, Raman spectroscopy, and X-ray photoelectron spectroscopy. Characterization techniques depict single-phase $LiNi_{1/3}Co_{1/3}Mn_{1/3}O_2$ with particle sizes in the range of 220−280 nm. Electrochemical studies on $LiNi_{1/3}Co_{1/3}Mn_{1/3}O_2$ and $LiNi_{1/3}Co_{1/3}Mn_{1/3}O_2$—graphene were conducted using cyclic voltammetry, galvanostatic charge−discharge, and electrochemical impedance spectroscopy methods by constructing a lithium half-cell. Cyclic voltammograms show the well-defined redox peaks corresponding to Ni^{2+}/Ni^{4+}. Charge−discharge tests were performed at different *C* rates: 0.05, 1, and 5 between 2.5 and 4.4 V. The results indicate the better electrochemical performance of the $LiNi_{1/3}Co_{1/3}Mn_{1/3}O_2$—graphene composite in terms of high discharge capacity (188 mAh/g), good rate capability, and good cycling performance compared to $LiNi_{1/3}Mn_{1/3}Co_{1/3}O_2$. The improved electrochemical performance of the $LiNi_{1/3}Co_{1/3}Mn_{1/3}O_2$—graphene composite is attributed to a decrease in the charge-transfer resistance.

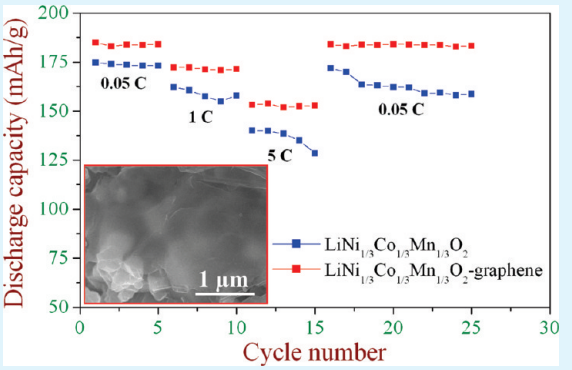

KEYWORDS: $LiNi_{1/3}Co_{1/3}Mn_{1/3}O_2$, graphene, conductive additive, cathode, lithium-ion battery, rate capability

1. INTRODUCTION

Lithium-ion batteries (LIBs), which use the lithium transition-metal oxides as the positive electrode, have become attractive energy storage systems for portable electronic devices and the powering of emission-free vehicles.[1−6] Among the lithium transition-metal oxide intercalation compounds, $LiCoO_2$ has been adopted as the cathode material in commercial LIBs because of its high specific capacity, long cyclic stability, and easy preparation.[7−10] However, the low thermal stability and high cost of $LiCoO_2$ shifted the research efforts toward the search for alternative cathodes, such as layer-structured $LiNiO_2$ (high reversible capacity but low thermal stability) and spinel-structured $LiMn_2O_4$ (high thermal stability and low cost but low reversible capacity).[4,5] As an alternative to $LiCoO_2$, lithium nickel manganese oxides have been extensively studied to take advantage of the lower cost and toxicity of nickel and manganese compared to cobalt and to overcome the above-mentioned disadvantages.[11,12] Nevertheless, it also has shown some drawbacks, such as the difficulty in preparation by a conventional solid-state method and low electronic conductivity.[13,14]

Structural stability and improved electronic conductivity in lithium nickel manganese oxides have been observed by the partial replacement of manganese and nickel by cobalt.[15,16] Among the various investigated $LiNi_xMn_yCo_{1-x-y}O_2$ series, $LiNi_{1/3}Mn_{1/3}Co_{1/3}O_2$ has been shown to be one of the most promising alternative cathode materials in terms of operating voltage, high specific capacity, cyclic stability, and structural stability.[17,18,4,5] However, the poor electronic conductivity of $LiNi_{1/3}Co_{1/3}Mn_{1/3}O_2$ resulted in a low electrochemical performance and limited its practical applications. To improve the electronic conductivity and thereby its performance, many attempts such as the addition of dopants or modification of the surface of $LiNi_{1/3}Mn_{1/3}Co_{1/3}O_2$ by coating with various materials like Al_2O_3, $AlPO_4$, $LiAlO_2$, carbon, etc., have been directed.[20−23] Many research works confirmed that dispersion of the active material in a highly conductive matrix, especially nanostructured carbon materials, would improve the electronic conductivity and thereby enhance the discharge capacities as well as cyclability at high current densities.[20−24]

Owing to its high electronic conductivity, large surface area, and excellent structural stability, graphene has emerged as a conductive medium for the development of highly efficient LIB electrodes.[25−30] Also, graphene is known to show large reversible capacities due to increased basal spacing.[28] The uses of graphene

Received: April 6, 2011
Accepted: June 29, 2011
Published: June 29, 2011

to form composite materials with $LiFePO_4$ have also been reported to improve the surface conductivity, capacity, rate capability, and cyclic stability of electrode materials.[31,32] Recently, we have been successful in demonstrating enhanced lithium-ion storage properties in nitrogen-doped graphene sheets compared to pristine graphene sheets synthesized by chemical vapor deposition techniques.[33] We have also shown enhanced fuel-cell performance with graphene-supported platinum and Pt_3M (M = Co and Cr) alloy nanoparticles.[34] In the present work, the use of graphene as a conductive additive to enhance the discharge capacity and rate capability of $LiNi_{1/3}Co_{1/3}Mn_{1/3}O_2$ electrode material is demonstrated.

2. EXPERIMENTAL SECTION

2.1. Preparation of Pure Graphene. High-quality graphene powder was prepared from graphite powder (Aldrich) in a two-step process, consisting of oxidation and/or exfoliation of graphite to graphite oxide (GO_x) by Hummer's method and chemical reduction of GO_x to graphene according to our previous publication.[35] The composition (wt %) of graphene was determined to be as follows: C, 99.3; O, <0.5; H, <3.8; N, <0.5.

2.2. Preparation of $LiNi_{1/3}Co_{1/3}Mn_{1/3}O_2$ and the $LiNi_{1/3}Co_{1/3}Mn_{1/3}O_2$−Graphene Composite. The materials were prepared according to the inverse microemulsion method described in ref 23. The conditions were modified to prepare single-phase $LiNi_{1/3}Co_{1/3}Mn_{1/3}O_2$ with good crystallinity. The microemulsion system used in this study consisted of lithium dodecylsulfate (LDS) as a surfactant, *n*-butanol as a cosurfactant, cyclohexane as an oil phase, and a Li−Ni−Co−Mn precursor solution as a dispersed aqueous phase. In a typical procedure, 102.4 mL of cyclohexane, 0.45 g of LDS, and 12.4 mL of *n*-butanol were mixed together and stirred well. A small portion of *n*-butanol (approximately 0.3 mL) was added until it turned transparent. Thereafter, stoichiometric amounts of aqueous transition-metal nitrate solutions [5 mL each of 1 M $Ni(NO_3)_2$, 1 M $Co(NO_3)_2$, and 1 M $Mn(NO_3)_2$] and 8.7 mL of 2 M $LiNO_3$ were added simultaneously at a flow rate of 0.5 mL/min and stirred for 6 h. The resulting suspension was stirred for 10 h and evaporated to form a gelatinous material. It was then calcined at 773 K for 4 h and ground into a fine powder. Finally, the material was calcined again at 1173 K for 8 h. For preparation of the $LiNi_{1/3}Co_{1/3}Mn_{1/3}O_2$−graphene composite, an ultrasonicated suspension of graphene powder (100 mg) in ethanol (10 mL) was added to the mixture to give a $LiNi_{1/3}Co_{1/3}Mn_{1/3}O_2$−graphene weight ratio of 90:10 and ball-milled under an argon atmosphere for 40 min. The milling experiments were performed in a Fritsch P5 planetary ball mill at a speed of 300 rpm using a tungsten carbide vial and tungsten carbide balls. A ball-to-mixture weight ratio was 30:1. Thereafter, the material was dried overnight at 393 K.

2.3. Characterization Techniques. X-ray diffraction (XRD) and scanning electron microscopy (SEM) were used for phase identification and for determination of the particle size, respectively. XRD measurements were performed on a Rigaku D/Max Ultima II X-ray diffractometer using a Cu Kα source operated at a scan rate of 0.1°/min over the 2θ range of 15−70°. SEM images were obtained using a JEOL JSM-6480LV system operated with an accelerating voltage of 20 kV. A high-resolution transmission electron microscope (JEOL 2010) was used to determine the lattice spacing of the materials. Micro-Raman scattering experiments were performed on a ISA Jobin-Yvon Inc. model T64000 FT-Raman at room temperature in a quasi-backscattering geometry with parallel polarization incident light. The excitation source used was an argon-ion laser operating at 514.532 nm, and measurements were performed at a laser incident power of 0.3 mW. Extreme care was taken to avoid sample damage or laser-induced heating. An inductively coupled plasma mass spectroscopy (ICP-MS) method was used to determine the ion content in the metal oxide.

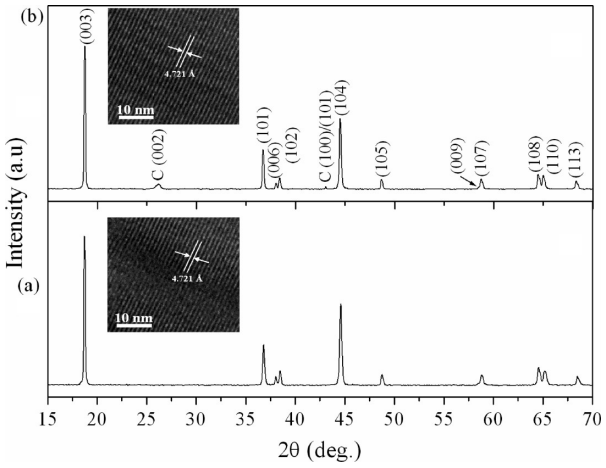

Figure 1. Powder XRD patterns of (a) $LiNi_{1/3}Co_{1/3}Mn_{1/3}O_2$ and (b) $LiNi_{1/3}Co_{1/3}Mn_{1/3}O_2$−graphene.

Electrochemical measurements were performed in a two-electrode coin cell (CR-2032) assembled with $LiNi_{1/3}Co_{1/3}Mn_{1/3}O_2$/$LiNi_{1/3}Co_{1/3}Mn_{1/3}O_2$−graphene as the cathode and lithium metal foil as counter and reference electrodes using a multichannel ARBIN BT 2010 battery-testing unit. The electrodes were prepared by coating the slurry of a mixture composed of 85 wt % active material, 8 wt % acetylene black, and 7 wt % polyvinylidene fluoride onto cleaned and polished aluminum foil. Subsequently, the electrodes were dried at 80 °C under vacuum for 24 h and pressed under 20 MPa of pressure. The weight of active material in the electrode was 8 mg/cm^2. The cells were assembled in an argon-filled glovebox (O_2, H_2O < 1 ppm). The electrolyte was 1 M $LiPF_6$ in a mixture of 1:1 (v/v) ethylene carbonate and dimethyl carbonate. A polypropylene film (Cellgard 2300) was used as the separator. Cyclic voltammograms (CVs) were recorded in the voltage range 2.5−4.4 V at a scanning rate of 0.05 mV/s. Galvanostatic charge−discharge tests were performed at *C* rates of 0.05, 1, and 5 in the voltage range 2.5−4.4 V. The potential values mentioned in the text are with respect to Li/Li^+.

3. RESULTS AND DISCUSSION

The inverse microemulsion method is a suitable method to generate metal colloids and/or clusters on the nanoscale with greater uniformity and controllable composition.[36] Micellar solutions are transparent, isotropic, thermodynamically stable water-in-oil microemulsions with nanosized water droplets that are dispersed in a continuous oil phase and stabilized by surfactant molecules at the water/oil interface. The greater degree of mixing achieved through microemulsion methods eliminates the need for long-range diffusion of ions, making only a local rearrangement necessary for product formation. Mixing of the microemulsions and evaporation at 343 K resulted in the formation of a gel consisting of metal nitrates in narrow regions, which were surrounded by surfactant molecules. During subsequent heat treatment of the gel at high temperatures, the formation of $LiNi_{1/3}Co_{1/3}Mn_{1/3}O_2$ particles results.

Powder XRD patterns of $LiNi_{1/3}Co_{1/3}Mn_{1/3}O_2$ and $LiNi_{1/3}Co_{1/3}Mn_{1/3}O_2$−graphene are shown in Figure 1. All diffraction peaks are sharp and well-defined, suggesting that the prepared compounds are well-crystallized. Both materials are indexed to the hexagonal α-$NaFeO_2$ crystal structure with a space group

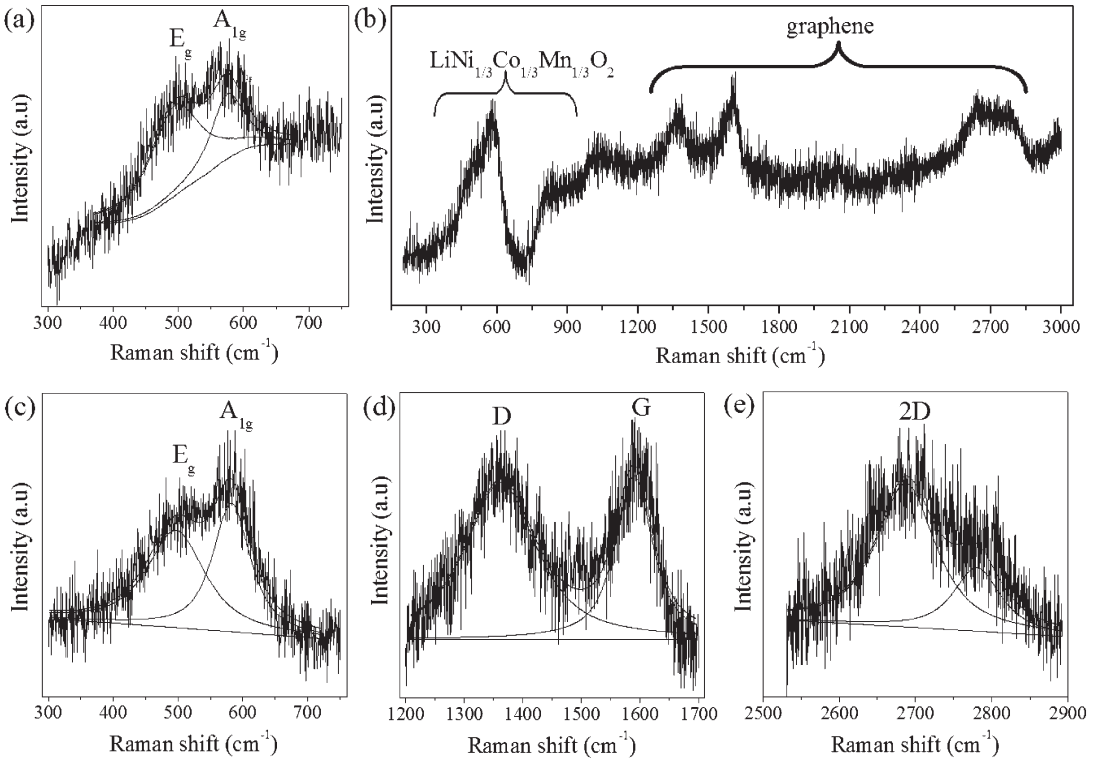

Figure 2. Raman spectra at 514 nm for $LiNi_{1/3}Co_{1/3}Mn_{1/3}O_2$ and $LiNi_{1/3}Co_{1/3}Mn_{1/3}O_2$−graphene: (a) pristine $LiNi_{1/3}Co_{1/3}Mn_{1/3}O_2$; (b) a $LiNi_{1/3}Co_{1/3}Mn_{1/3}O_2$−graphene composite in the range 300−3000 cm^{-1}; and (c−e) spectra in the region of $LiNi_{1/3}Co_{1/3}Mn_{1/3}O_2$, graphene D and G bands and a graphene 2D band, respectively.

of *R*3*m*. The calculated lattice constants (*a* and *c*) for both $LiNi_{1/3}Co_{1/3}Mn_{1/3}O_2$ (*a* = 2.851 Å and *c* = 14.219 Å) and $LiNi_{1/3}Co_{1/3}Mn_{1/3}O_2$−graphene (*a* = 2.857 Å and *c* = 14.227 Å) are similar and are in good agreement with the literature values.[17,19,23] The clear splitting of hexagonal doublets (0 0 6)/(0 1 2) and (1 0 8)/(1 1 0) near 38° and 65° observed for both of these samples indicates the highly ordered layer structure of $LiNi_{1/3}Co_{1/3}Mn_{1/3}O_2$.[19] The integrated intensity ratio of the (0 0 6):(1 0 2) lines in the XRD patterns is determined to be 1.33 and 1.37 for $LiNi_{1/3}Co_{1/3}Mn_{1/3}O_2$ and the $LiNi_{1/3}Co_{1/3}Mn_{1/3}O_2$−graphene composite, respectively. This is indicative of a highly ordered hexagonal lattice with lithium ions at the 3a site, transition-metal ions (Ni, Co, and Mn) at the 3b site, and oxygen ions at the 6c site.[19] From the XRD pattern of $LiNi_{1/3}Co_{1/3}Mn_{1/3}O_2$−graphene, the additional peaks around 26° and 47° are attributed to the (0 0 2) and (1 0 0)/(1 0 1) planes of the hexagonal graphite structure.[33−35] The high-resolution transmission electron microscopy images of $LiNi_{1/3}Co_{1/3}Mn_{1/3}O_2$ and $LiNi_{1/3}Co_{1/3}Mn_{1/3}O_2$−graphene shown in the inset in Figure 1 reveal well-defined lattice fringes with a separation of 4.721 Å, which corresponds to the (0 0 3) plane.

First-order Raman spectra recorded for the materials are shown in Figure 2. The deconvoluted spectra of $LiNi_{1/3}Co_{1/3}Mn_{1/3}O_2$ (Figure 2a) and the $LiNi_{1/3}Co_{1/3}Mn_{1/3}O_2$−graphene composite (Figure 2c) clearly show two bands at 500 and 580 cm^{-1}. These two bands are assigned to E_g and A_{1g} Raman-active modes for the transition metal−oxygen arrangements in the layered lithium metal oxide with rhombohedral *R*3*m* symmetry.[37,38] The absence of the characteristic cubic spinel band at 630 cm^{-1} indicates that the prepared materials are single-phase layered materials.[37] Thus, the Raman spectral data underpinned the XRD results. The Raman spectrum recorded for the $LiNi_{1/3}Co_{1/3}Mn_{1/3}O_2$−graphene composite in the range 300−3000 cm^{-1} is shown in Figure 2b. The Raman peaks corresponding to both the $LiNi_{1/3}Co_{1/3}Mn_{1/3}O_2$ and graphene are observed. The bands corresponding to the graphene are deconvoluted and shown in Figure 2d,e. The intense peaks observed at ∼1352 and ∼1590 cm^{-1} correspond to the D and G bands of graphene, respectively. The D band arises because of the disorder induced in sp^2-bonded carbon, whereas the G band arises from the in-plane vibration of sp^2 carbon atoms of graphene. A 2D band, which is the characteristic band of graphene, is usually used to determine the number of layers of graphene in the sample. This band originated from a two-phonon double-resonance Raman process associated with the band structure of graphene. A 2D band observed at 2695 ± 5 cm^{-1} (Figure 2e) in different regions indicates that the composite has 2−5 layers of graphene.[39] The metal ion content in $LiNi_{1/3}Co_{1/3}Mn_{1/3}O_2$ measured by ICP-MS experiment is Li:Ni:Co:Mn = 1.031:0.334:0.327:0.337. The observed values are in good agreement with the starting material composition within error limits.

The surface morphologies of graphene, $LiNi_{1/3}Co_{1/3}Mn_{1/3}O_2$, and $LiNi_{1/3}Co_{1/3}Mn_{1/3}O_2$−graphene active materials studied by SEM and transmission electron microscopy (TEM) are shown in Figure 3. Micron-size corrugated and transparent graphene sheets can be seen from SEM and TEM (Figure 3a, a1,a2). Agglomerated polyhedral-shaped particles with sizes of 220−280 nm are observed from the low- and high-magnification SEM images of $LiNi_{1/3}Co_{1/3}Mn_{1/3}O_2$ (Figure 3b,b1). The low-magnification SEM image of the $LiNi_{1/3}Co_{1/3}Mn_{1/3}O_2$−graphene composite shows the polyhedral-shaped particles wrapped between the graphene sheets as well as particles embedded in the graphene sheets (Figure 3c,c1). The high-magnification

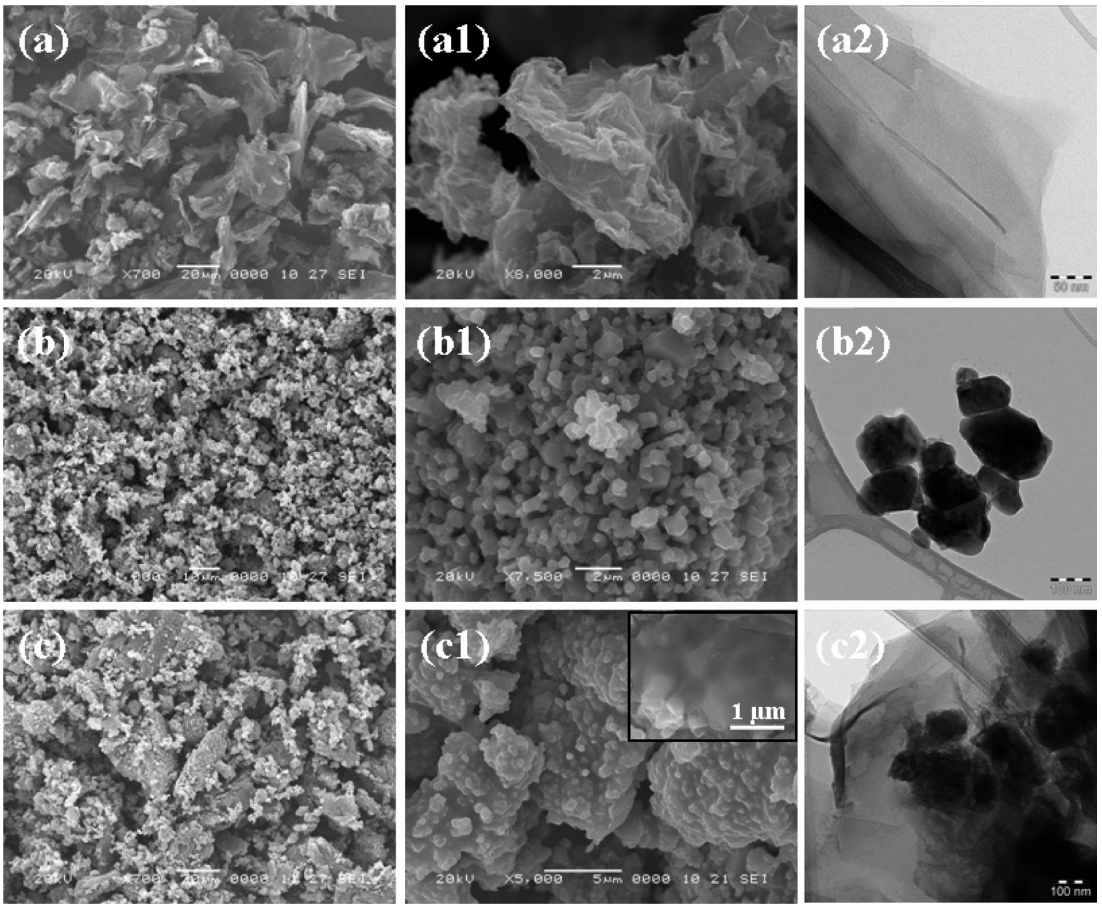

Figure 3. Low-magnification SEM (left), high-magnification SEM (middle), and TEM (right) images of graphene (a, a1, and a2), $LiNi_{1/3}Co_{1/3}Mn_{1/3}O_2$ (b, b1, and b2), and $LiNi_{1/3}Co_{1/3}Mn_{1/3}O_2$−graphene (c, c1, and c2).

image presented in the inset in Figure 3c1 depicts the 200−250-nm-sized particles covered with a transparent graphene sheet. The average particle sizes obtained from the TEM images are 80−120 and 70−110 nm for $LiNi_{1/3}Co_{1/3}Mn_{1/3}O_2$ (Figure 3b2) and $LiNi_{1/3}Co_{1/3}Mn_{1/3}O_2$−graphene (Figure 3c2), respectively.

To gain more insight into the oxidation state of transition metals in the layered $LiNi_{1/3}Co_{1/3}Mn_{1/3}O_2$ materials, X-ray photoelectron spectroscopy (XPS) measurements were performed, and the corresponding spectra are presented in Figure 4. The peaks at binding energies of 854, 780, and 642 eV are attributed to Ni^{2+}, Co^{3+}, and Mn^{4+} respectively, in $LiNi_{1/3}Co_{1/3}Mn_{1/3}O_2$.[17,23] The observed C 1s peak at 285 eV in the graphene-based composite mainly represents graphitic carbon.[30,32] The observed XPS peaks of the $LiNi_{1/3}Co_{1/3}Mn_{1/3}O_2$−graphene composite are identical with those of $LiNi_{1/3}Co_{1/3}Mn_{1/3}O_2$, which indicates that the ball-milling process does not affect the oxidation states of nickel, cobalt, and manganese. In the case of pristine $LiNi_{1/3}Co_{1/3}Mn_{1/3}O_2$, a small feature is observed at a binding energy of 288.7 ± 0.2 eV. It is attributed to the presence of −O−C−O− functional groups. A negligible amount of amorphous carbon with these functional groups originates from the reactants used in the preparation of $LiNi_{1/3}Co_{1/3}Mn_{1/3}O_2$. It is likely that pyrolysis of metal precursors/organic molecules adsorbed on $LiNi_{1/3}Co_{1/3}Mn_{1/3}O_2$ particles during the synthesis causes the formation of a negligible amount of carbon.

CVs recorded for the $LiNi_{1/3}Co_{1/3}Mn_{1/3}O_2$−graphene composite in the voltage range 2.5−4.4 V at a scanning rate of 0.05 mV/s are shown in Figure 5. The CVs show well-defined redox peaks, with an anodic peak centered at 3.85 V and the corresponding cathodic peak at 3.65 V. These peaks correspond to the Ni^{2+}/Ni^{4+} redox couple.[17] The absence of a reduction peak at 3.2 V indicates that there is no reduction of Mn^{3+}/Mn^{4+}. It is accepted in the literature that nickel and cobalt with oxidation states 2+ and 3+, respectively, are known to be electrochemically active and undergo redox transitions during charge−discharge cycles, whereas manganese with oxidation state 4+ is not active, and this is believed to increase the stability of the metal oxide lattice.[18,19] Except for the first cycle, all of the curves in the subsequent cycles follow the same path. This indicates the good (de-)intercalation of lithium ions in the prepared $LiNi_{1/3}Co_{1/3}Mn_{1/3}O_2$−graphene electrode material. The higher current observed for the $LiNi_{1/3}Co_{1/3}Mn_{1/3}O_2$−graphene composite compared to pristine $LiNi_{1/3}Co_{1/3}Mn_{1/3}O_2$ indicates an improvement in the electrochemical properties by graphene addition (Figure S1, Supporting Information).

To study the rate capability of the fabricated electrodes, the cells were charged and discharged at various current rates. Galvanostatic charge−discharge curves of $LiNi_{1/3}Co_{1/3}Mn_{1/3}O_2$ and the $LiNi_{1/3}Co_{1/3}Mn_{1/3}O_2$−graphene composite at *C* rates of 0.05, 1, and 5 in the voltage range between 2.5 and 4.4 V are shown in Figure 6. Though there is a decrease in the discharge

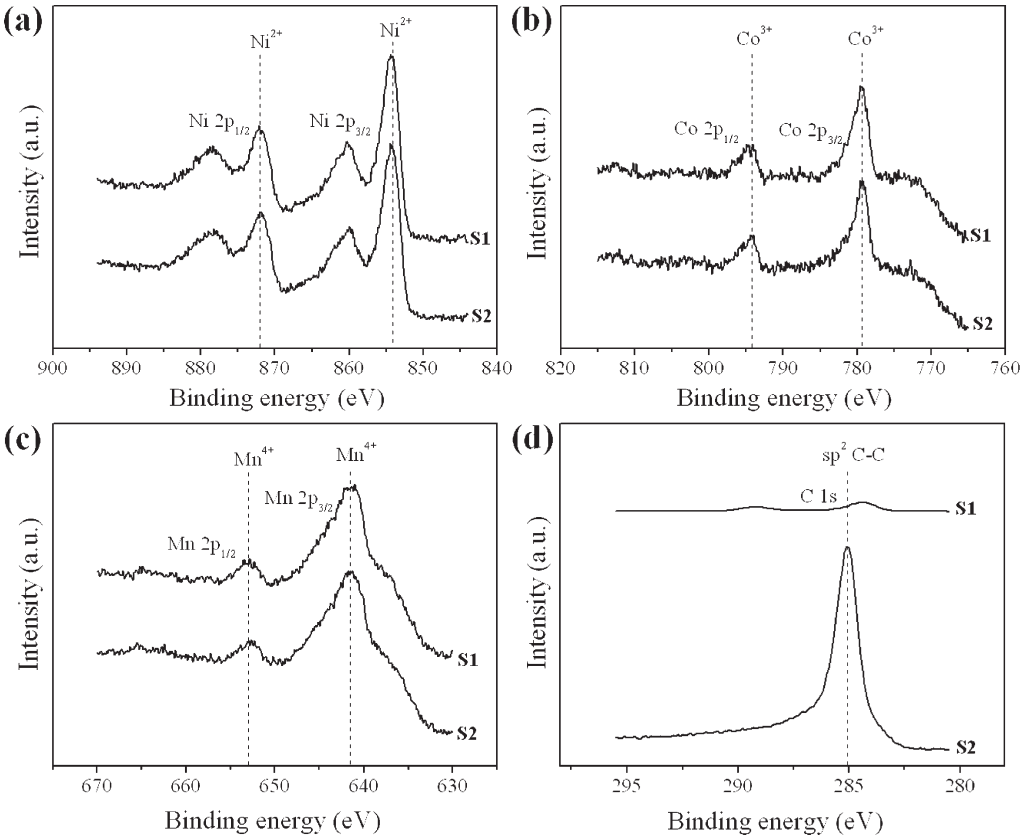

Figure 4. XPS spectra of Ni 2p, Co 2p, Mn 2p, and C 1s for $LiNi_{1/3}Co_{1/3}Mn_{1/3}O_2$ (S1) and the $LiNi_{1/3}Co_{1/3}Mn_{1/3}O_2$—graphene composite (S2).

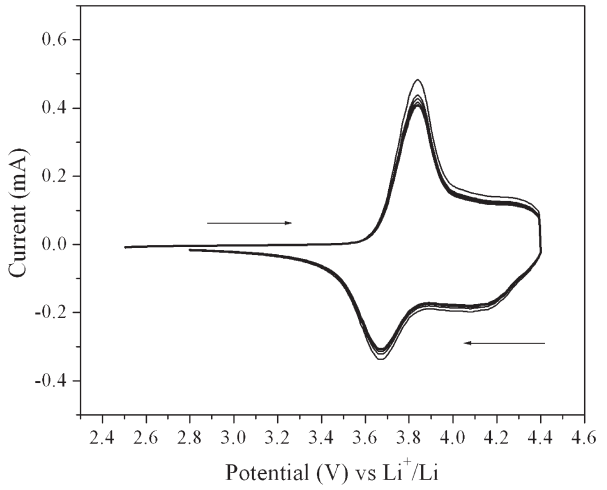

Figure 5. CV of the $LiNi_{1/3}Co_{1/3}Mn_{1/3}O_2$—graphene composite in the voltage range between 2.5 and 4.4 V; scan rate −0.05 mV/s.

capacity of both samples upon increasing current rates, the $LiNi_{1/3}Co_{1/3}Mn_{1/3}O_2$ electrode clearly shows more a prominent decrease in the discharge capacity. The charge—discharge capacities observed with the electrodes are depicted in Table S1 (Supporting Information). The initial charge—discharge capacities observed for $LiNi_{1/3}Co_{1/3}Mn_{1/3}O_2$ at *C* rates of 0.05, 1, and 5 are 184/174, 171/162, and 149/138 mAh/g, respectively. However, the discharge capacity falls to 173, 157, and 128 mAh/g (at current rates of 0.05, 1, and 5, respectively) after the fifth charge—discharge cycle. In the case of the $LiNi_{1/3}Co_{1/3}Mn_{1/3}O_2$—graphene composite electrode, the initial charge—discharge capacities at *C* rates of 0.05, 1, and 5 are 188/185, 178/172, and 161/153 mAh/g, respectively, and the discharge capacity is retained after five cycles. It is worth pointing out that the $LiNi_{1/3}Co_{1/3}Mn_{1/3}O_2$—graphene composite exhibited high discharge capacities at 0.05, 1, and 5 current rates and also less irreversible capacity losses when compared to $LiNi_{1/3}Mn_{1/3}Co_{1/3}O_2$. The discharge capacity observed with the $LiNi_{1/3}Co_{1/3}Mn_{1/3}O_2$—graphene composite as the cathode is higher than that observed with $LiFePO_4$—graphene as the cathode.[31,32]

The extended cyclic stability measurements of $LiNi_{1/3}Co_{1/3}Mn_{1/3}O_2$ and the $LiNi_{1/3}Co_{1/3}Mn_{1/3}O_2$—graphene composite electrodes conducted at different current rates are shown in Figure 7. Initially, charge—discharge measurements on both of the samples were conducted at a *C* rate of 0.05, increased to a *C* rate of 5 stepwise, and finally returned back to 0.05. The $LiNi_{1/3}Co_{1/3}Mn_{1/3}O_2$—graphene composite showed a very stable capacity even at high current rates, whereas $LiNi_{1/3}Co_{1/3}Mn_{1/3}O_2$ showed a drastic fall in the specific capacity when cycled at higher *C* rates of 1 and 5. The capacity fading observed for $LiNi_{1/3}Co_{1/3}Mn_{1/3}O_2$ at high current rates was ascribed to the polarization effect. Returning to the low current rate (*C* rate of 0.05), the nominal capacity of the $LiNi_{1/3}Co_{1/3}Mn_{1/3}O_2$—graphene composite is retained with 99.1%. In contrast, $LiNi_{1/3}Co_{1/3}Mn_{1/3}O_2$ exhibited poor capacity retention (only 89.7%). The high rate capability of the composite is due to the increase in the electronic conductivity, which reduces the cell polarization and prevents the evolution of oxygen from the cathodes at the end of charge.

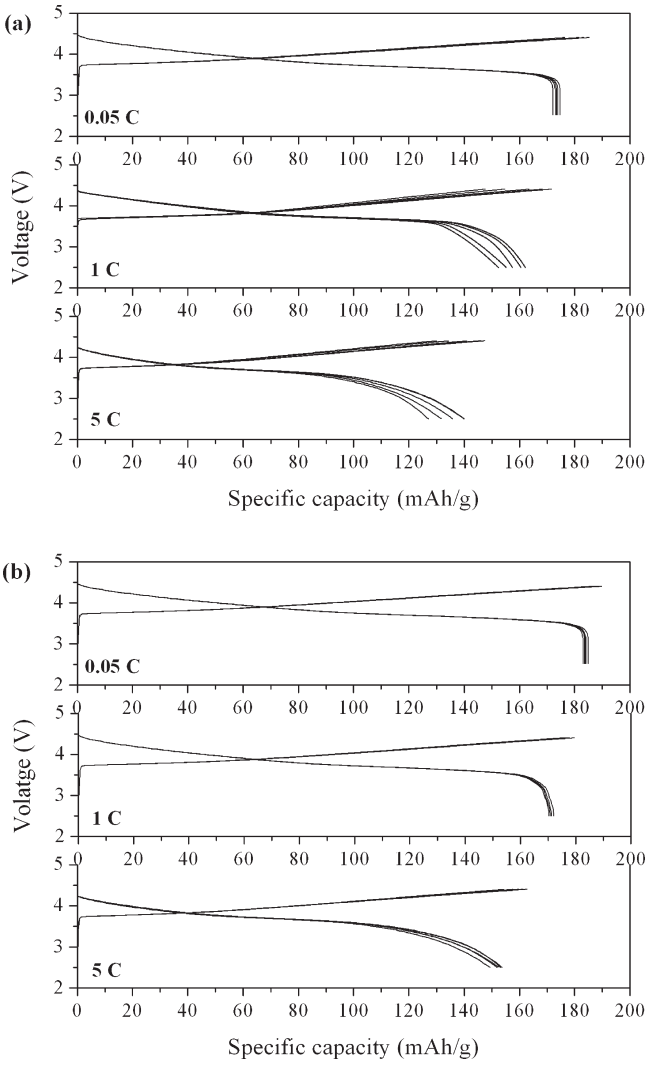

Figure 6. Charge−discharge curves of (a) $LiNi_{1/3}Co_{1/3}Mn_{1/3}O_2$ and (b) $LiNi_{1/3}Co_{1/3}Mn_{1/3}O_2$−graphene at *C* rates of 0.05, 1, and 5 in the voltage range between 2.5 and 4.4 V.

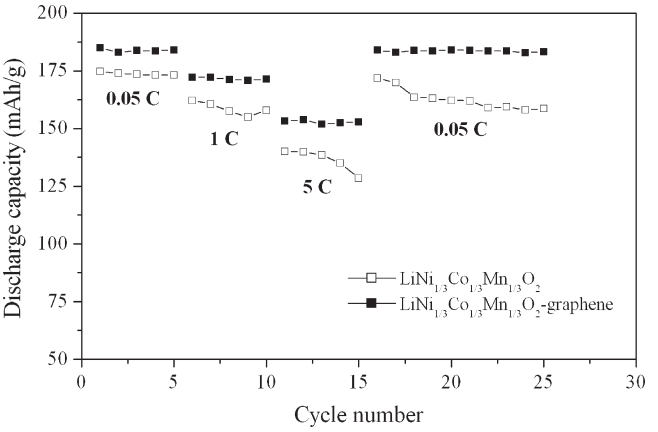

Figure 7. Cycling performance of $LiNi_{1/3}Co_{1/3}Mn_{1/3}O_2$ and $LiNi_{1/3}Co_{1/3}Mn_{1/3}O_2$−graphene at different discharge rates, 0.05, 1, and 5, in the voltage range between 2.5 and 4.4 V.

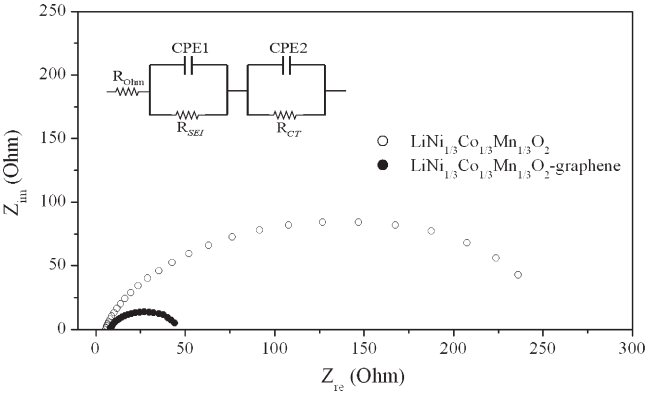

Figure 8. AC impedance spectra of $LiNi_{1/3}Co_{1/3}Mn_{1/3}O_2$ and $LiNi_{1/3}Co_{1/3}Mn_{1/3}O_2$−graphene in the frequency range from 100 kHz to 0.01 Hz. The inset figure shows the equivalent circuit for the EIS measurement.

To understand the beneficial effect of graphene on the electrochemical performance of $LiNi_{1/3}Co_{1/3}Mn_{1/3}O_2$, alternating-current (AC) impedance measurements are carried out after five charge−discharge cycles at 0.05 and the corresponding Nyquist plots are shown in Figure 8. A dramatic decrease in the area of the semicircle, which reflects the charge-transfer resistance, is observed for the $LiNi_{1/3}Co_{1/3}Mn_{1/3}O_2$−graphene composite electrode compared to $LiNi_{1/3}Co_{1/3}Mn_{1/3}O_2$. The impedance plots show a high-frequency intercept at the Z_{re} axis and a broad depressed semicircle. The high-frequency intercept is due to the ohmic resistance (R_{ohm}). The depressed semicircle in the high- and low-frequency regions is related to the formation of a surface layer on the active material and the intercalation/deintercalation of lithium ions into/from the electrodes. An equivalent circuit used to fit the spectra is shown in the inset. The parameters R_{SEI} and CPE1 correspond to the surface layer resistance and capacitance, whereas R_{CT} and CPE2 correspond to the lithium intercalation/deintercalation process and interfacial capacitance, respectively. R_{CT} is calculated as 181 and 32 Ω for the pristine and graphene-based composite electrodes, respectively. The enhanced electronic/ionic conductivity observed for the $LiNi_{1/3}Co_{1/3}Mn_{1/3}O_2$−graphene composite entails an increased discharge capacity and a high rate capability, facilitating the transfer of lithium ions across the active material/electrolyte interface, as well as the transfer of electrons from the current collector to the active material. In addition, the factors that may have contributed to the superior electrochemical performance of the $LiNi_{1/3}Co_{1/3}Mn_{1/3}O_2$−graphene composite electrode are improvement in the structural stability, a decrease in the disorder of metal ions in the lattice, suppression of the dissolution of transition-metal ions and phase transitions, removal of HF from the electrolyte solution, and a reduced amount of heat production during charge−discharge processes. The results demonstrate that the $LiNi_{1/3}Co_{1/3}Mn_{1/3}O_2$−graphene composite is suitable for application in advanced rechargeable lithium-ion batteries.

4. CONCLUSIONS

$LiNi_{1/3}Co_{1/3}Mn_{1/3}O_2$ prepared by the microemulsion route was used to make a composite with graphene by ball milling. Layer-structured $LiNi_{1/3}Co_{1/3}Mn_{1/3}O_2$ with good hexagonal ordering was evident from XRD and Raman studies. According

to the electrochemical studies, the composite delivered the highest discharge capacity at different *C* rates when compared to $LiNi_{1/3}Co_{1/3}Mn_{1/3}O_2$. In addition, the composite showed a better capacity retention upon extended cycling at all of the *C* rates examined. The improved rate capability and cycling performance of the $LiNi_{1/3}Co_{1/3}Mn_{1/3}O_2$—graphene composite was attributed to an increase in the grain connectivity and high electronic conductivity.

■ ASSOCIATED CONTENT

Supporting Information. CVs of $LiNi_{1/3}Co_{1/3}Mn_{1/3}O_2$ and $LiNi_{1/3}Co_{1/3}Mn_{1/3}O_2$—graphene and a table detailing the charge—discharge capacities observed with the fabricated electrodes. This material is available free of charge via the Internet at http://pubs.acs.org.

■ AUTHOR INFORMATION

Corresponding Author
*E-mail: leela@rice.edu (A.L.M.R.), vrao.chitturi@ymail.com (C.V.R.).

■ ACKNOWLEDGMENT

C.V.R. and Y.I. are thankful for the support of NASA-EPSCoR under Grants NNX08AB12A and NNX09AV05A. A.L.M.R. and P.M.A. acknowledge funding support from the Army Research Office. The authors acknowledge the help of José J. Saavedra Arias for Raman spectra and Cristina Diaz Borrero for SEM measurements at the University of Puerto Rico.

■ REFERENCES

(1) Armand, M.; Tarascon, J.-M. *Nature* **2008**, *451*, 652–657.
(2) Whittingham, M. S. *Chem. Rev.* **2004**, *104*, 4271–4301.
(3) *Advances in lithium-ion batteries*; Van Schalkwijk, W., Scrosati, B., Eds.; Kluwer Academic/Plenum: New York, 2002.
(4) Ellis, B. L.; Lee, K. T.; Nazar, L. F. *Chem. Mater.* **2010**, *22*, 691–714.
(5) Goodenough, J. B.; Kim, Y. *Chem. Mater.* **2010**, *22*, 587–603.
(6) Tarascon, J.-M.; Armand, M. *Nature* **2001**, *414*, 359–367.
(7) Mizushima, K.; Jones, P. C.; Wiseman, P. J.; Goodenough, J. B. *Mater. Res. Bull.* **1980**, *15*, 783–789.
(8) Plichta, E. J.; Slane, S.; Uchiyama, M.; Salomon, M.; Chua, D.; Ebner, W. B.; Lin, H. W. *J. Electrochem. Soc.* **1989**, *136*, 1865–1869.
(9) Reimers, J. N.; Dahn, J. *J. Electrochem. Soc.* **1992**, *139*, 2091–2097.
(10) Gummow, R. J.; Thackeray, M. M.; David, W. I. F.; Hull, S. *Mater. Res. Bull.* **1992**, *27*, 327–337.
(11) Lu, Z.; Dahn, J. R. *J. Electrochem. Soc.* **2000**, *149*, A815–A822.
(12) Kim, J.-H.; Yoon, C. S.; Sun, Y.-K. *J. Electrochem. Soc.* **2003**, *150*, A538–A542.
(13) Yoshio, M.; Todorov, Y.; Yamato, K.; Noguchi, H.; Itoh, J.; Okada, M.; Mouri, T. *J. Power Sources* **1998**, *74*, 46–53.
(14) Cushing, B. L.; Goodenough, J. B. *Solid State Sci.* **2002**, *4*, 1487–1493.
(15) Ohzuku, T.; Makimura, Y. *Chem. Lett.* **2001**, *30*, 642–643.
(16) Yabuuchi, N.; Ohzuku, T. *J. Power Sources* **2003**, *119*, 171–174.
(17) Shaju, K. M.; Subba Rao, G. V.; Chowdari, B. V. R. *Electrochim. Acta* **2002**, *48*, 145–151.
(18) Kim, J.-M.; Chung, H.-T. *Electrochim. Acta* **2004**, *49*, 3573–3580.
(19) Hwang, B. J.; Tsai, Y. W.; Carlier, D.; Ceder, G. *Chem. Mater.* **2003**, *15*, 3676–3682.
(20) Kim, Y.; Kim, H.; Martin, S. W. *Electrochim. Acta* **2006**, *52*, 1316–1322.
(21) Cho, J.; Kim, Y.-W.; Kim, B.; Lee, J.-G.; Park, B. *Angew. Chem., Int. Ed.* **2003**, *42*, 1618–1621.
(22) Kim, H.; Kim, Y.; Kim, S.; Martin, S. W. *J. Power Sources* **2006**, *161*, 623–627.
(23) Sinha, N. N.; Munichandraiah, N. *ACS Appl. Mater. Interfaces* **2009**, *1*, 1241–1249.
(24) Ban, C.; Li, Z.; Wu, Z.; Kirkham, M. J.; Chen, L.; Jung, Y. S.; Payzant, E. A.; Yan, Y.; Whittingham, M. S.; Dillon, A. C. *Adv. Energy Mater.* **2011**, *1*, 58–62.
(25) Geim, A. K.; Novoselov, K. S. *Nat. Mater.* **2007**, *6*, 183–191.
(26) Su, F.-Y.; You, C.; He, Y.-B.; Lv, W.; Cui, W.; Jin, F.; Li, B.; Yang, Q.-H.; Kang, F. *J. Mater. Chem.* **2010**, *20*, 9644–9650.
(27) Stoller, M. D.; Park, S. J.; Zhu, Y. W.; An, J. H.; Ruoff, R. S. *Nano Lett.* **2008**, *8*, 3498–3502.
(28) Yoo, E. J.; Kim, J.; Hosono, E.; Zhou, H. S.; Kudo, T.; Honma, I. *Nano Lett.* **2008**, *8*, 2277–2282.
(29) Paek, S. M.; Yoo, E.; Honma, I. *Nano Lett.* **2009**, *9*, 72–75.
(30) Wang, D. H.; Choi, D. W.; Li, J.; Yang, Z. G.; Nie, Z. M.; Kou, R.; Hu, D. H.; Wang, C. M.; Saraf, L. V.; Zhang, J. G.; et al. *ACS Nano* **2009**, *3*, 907–914.
(31) Ding, Y.; Jiang, Y.; Xu, F.; Yin, J.; Ren, H.; Zhuo, Q.; Long, Z.; Zhang, P. *Electrochem. Commun.* **2010**, *12*, 10–13.
(32) Zhou, X.; Wang, F.; Zhu, Y.; Liu, Z. *J. Mater. Chem.* **2011**, *21*, 3353–3358.
(33) Reddy, A. L. M.; Srivastava, A.; Gowda, S. R.; Gullapalli, H.; Dubey, M.; Ajayan, P. M. *ACS Nano* **2010**, *4*, 6337–6342.
(34) Venkateswara Rao, Ch.; Reddy, A. L. M.; Ishikawa, Y.; Ajayan, P. M. *Carbon* **2010**, *49*, 931–936.
(35) Gao, W.; Alemany, L. B.; Ci, L.; Ajayan, P. M. *Nat. Chem.* **2009**, *1*, 403–408.
(36) Venkateswara Rao, Ch.; Viswanathan, B. *J. Phys. Chem. C* **2007**, *111*, 16538–16543.
(37) Inaba, M.; Iriyama, Y.; Ogumi, Z.; Todzuka, Y.; Tasaka, A. *J. Raman Spectrosc.* **1997**, *28*, 613–617.
(38) Saavedra-Arias, J. J.; Karan, N. K.; Pradhan, D. K.; Kumar, A.; Nieto, S.; Thomas, R.; Katiyar, R. S. *J. Power Sources* **2008**, *183*, 761–765.
(39) Ferrari, A. C.; Meyer, J. C.; Scardaci, V.; Casiraghi, C.; Lazzeri, M.; Mauri, F.; Piscanec, S.; Jiang, D.; Novoselov, K. S.; Roth, S.; Geim, A. K. *Phys. Rev. Lett.* **2006**, *97*, 187401-4.